A reduced graphene oxide/Co₃O₄ composite for supercapacitor electrode

Chengcheng Xiang [a,b], Ming Li [a], Mingjia Zhi [a], Ayyakkannu Manivannan [c], Nianqiang Wu [a,*]

[a] Department of Mechanical and Aerospace Engineering, West Virginia University, Morgantown, WV 26506-6106, USA
[b] Department of Industrial and Management Systems Engineering, West Virginia University, Morgantown, WV 26506-6107, USA
[c] National Energy Technology Laboratory, U.S. Department of Energy, Morgantown, WV 26507, USA

HIGHLIGHTS

► Co₃O₄ nanoparticles are *in-situ* grown on the chemically reduced graphene oxide.
► The composite exhibits high rate capability and excellent long-term stability.
► The composite supercapacitor electrode has high energy density and power density.

ARTICLE INFO

ABSTRACT

20 nm sized Co₃O₄ nanoparticles are *in-situ* grown on the chemically reduced graphene oxide (rGO) sheets to form a rGO–Co₃O₄ composite during hydrothermal processing. The rGO–Co₃O₄ composite is employed as the pseudocapacitor electrode in the 2 M KOH aqueous electrolyte solution. The rGO–Co₃O₄ composite electrode exhibits a specific capacitance of 472 F g^{-1} at a scan rate of 2 mV s^{-1} in a two-electrode cell. 82.6% of capacitance is retained when the scan rate increases to 100 mV s^{-1}. The rGO–Co₃O₄ composite electrode shows high rate capability and excellent long-term stability. It also exhibits high energy density at relatively high power density. The energy density reaches 39.0 Wh kg^{-1} at a power density of 8.3 kW kg^{-1}. The super performance of the composite electrode is attributed to the synergistic effects of small size and good redox activity of the Co₃O₄ particles combined with high electronic conductivity of the rGO sheets.

© 2012 Elsevier B.V. All rights reserved.

1. Introduction

Electrochemical capacitors (also called supercapacitors) are characteristic of high power density, fast charge–discharge and long lifetime, which serve as energy storage devices complementary to batteries [1–3,19]. Supercapacitors are generally classified into electrical double-layer capacitor (EDLC) and pseudocapacitor. EDLC supercapacitors store energy through the accumulated charge at the interface between an electrode and an electrolyte. The energy storage mechanism of EDLC allows for long-term stability and fast charge–discharge. Activated carbon powders are the typical materials used in currently commercial EDLC supercapacitors because of their high specific surface area, high thermal stability, high conductivity and excellent corrosion resistance to electrolyte [2]. Recently, graphene has emerged as a promising candidate for EDLC supercapacitors due to its

extremely high specific surface area, excellent electronic conductivity, outstanding intrinsic mechanical strength, reasonable chemical stability and superior thermal conductivity [4–7]. However, the energy density of graphene-based supercapacitors still cannot meet the current need. Generally, the energy density of currently commercial EDLC supercapacitors is typically 3–5 Wh kg^{-1}, which is much lower than that of an electrochemical battery (30–40 Wh kg^{-1} for a lead acid battery and 10–250 Wh kg^{-1} for a lithium-ion battery) [8,9]. Therefore, pseudocapacitors are being developed to improve the energy density of devices since pseudocapacitors store and deliver energy through redox reactions, leading to high specific capacitance [10,11]. Transition metal oxides such as MnO₂, NiO, Fe₂O₃ and Co₃O₄ are being studied as candidate materials for pseudocapacitor electrodes [10–17]. Although metal oxides alone offer high specific capacitance, they deliver low power density and poor rate capability (dramatic drop of specific capacitance with an increase at a high scan rate) due to poor electronic conductivity [18–21]. Pseudocapacitor electrodes made of metal oxides generally possess poor energy density especially at high power density.

* Corresponding author. Tel.: +1 304 293 3326.
  E-mail address: nick.wu@mail.wvu.edu (N. Wu).

In order to obtain high-performance supercapacitors for a specific application that requires both high power density and energy density, many approaches have been explored to obtain desirable electrode materials and structures [22–24]. According to the equations of $P = \Delta V^2/(4Rm)$ and $E = 1/2\, C\Delta V^2$, the power density (P) and the energy density (E) of supercapacitors can be improved by reducing the equivalent series resistance (R) and increasing the operating potential window (ΔV) as well as specific capacitance (C), respectively. Therefore, an efficient strategy to achieve high energy density without sacrificing the power density is to develop the composite materials that combine high conductivity of carbon materials with high specific capacitance of metal oxides [10]. In the present study, Co_3O_4 nanoparticles are therefore in-situ grown on the chemically reduced graphene oxide (rGO) sheets to form a rGO–Co_3O_4 composite. The Co_3O_4 nanoparticles serve as the active sites of redox reactions, which result in high specific capacitance. Because Co_3O_4 is a low electrically conductive material, it is made in the ultra-small size and in intimate contact with the highly conductive rGO sheet. As a result, the rGO–Co_3O_4 composites not only exhibit the pseudocapacitive behavior but also possess good electron transport capability. Hence the supercapacitor electrode made of the rGO–Co_3O_4 composite is expected to exhibit good rate capability and high energy density without sacrificing power density. In addition, large volume change occurs in Co_3O_4 during the course of charge/discharge [25]. Small sized Co_3O_4 nanoparticle supported on the graphene sheets that have high mechanical strength and toughness will mitigate this problem. As a result, the rGO–Co_3O_4 composite will show good cycling stability.

2. Experimental

2.1. rGO–Co_3O_4 composite synthesis

Graphene oxide (GO) was synthesized by exfoliation of graphite according to the well-established Hummers method [26,27]. 80 mg of GO was then dispersed into 24 mL of ethanol under ultrasonication for 1 h. 20 mg of $Co(CH_3COO)_2$ dissolved in 1.2 mL of deionized (DI) water was added, following by addition of 1.2 mL of DI water. The reaction was kept at 80 °C with stirring for 10 h. Subsequently, the reaction mixture was transferred to a 100 mL of Teflon-lined autoclave for hydrothermal treatment at 150 °C for 3 h. The product was centrifuged and washed with ethanol and water to obtain the rGO–Co_3O_4 composites. For the preparation of rGO, GO was hydrothermally treated at the same condition without the addition of $Co(CH_3COO)_2$.

2.2. Characterization

The samples were observed with a JEOL JEM 2100 transmission electron microscope (TEM) at an operating voltage of 200 kV. The phase of rGO–Co_3O_4 composite was characterized with a PANalytical X-ray diffractometer (XRD). Raman spectra were obtained using a Renishaw invia Raman spectrometer under an excitation of the 532 nm laser. X-ray photoelectron spectra (XPS) were acquired with a PHI 5000 Versa Probe system (Physical Electronics, MN). The Brunauer–Emmett–Teller (BET) specific surface area was acquired based on the nitrogen adsorption/desorption at 77 K using ASAP 2020-Physisorption analyzer. Thermogravimetric analysis (TGA) was performed on the rGO–Co_3O_4 composite in air at a heating rate of 5 °C min^{-1} with a Cahn TG-131 thermogravimetric analyzer.

2.3. Electrochemical measurement

The active materials, polyvinylidene fluoride (PVDF) and super-P (commercial carbon black) were mixed in a mass ratio of 8:1:1 in 1-methyl-2-pyrrolidone (NMP) under ultrasonication for 4 h. The mixture was then stirred for 12 h to form homogeneous slurry. The viscous slurry was then coated onto a nickel disk as the working electrode. The working electrode was dried in air, and then heated in a vacuum oven at 120 °C for 4 h to evaporate the solvent. The mass loading of the electrode materials on single electrode was about 0.8 mg.

Cyclic voltammetry (CV), electrochemical impedance spectroscopy (EIS) and constant galvanostatic charge–discharge were performed on a two-electrode cell with a Gamry Reference 3000 instrument. A 2 M KOH aqueous solution was used as the electrolyte and Celgard 3501was employed as the separator. The CV measurement was conducted at a potential window of 0–0.85 V. EIS measurements were performed at an AC amplitude of 5 mV in a frequency range from 0.01 Hz to 600 kHz. The specific capacitance was calculated from the CV curves according to the following equation [28]

$$C = \frac{A}{\Delta V \times \nu \times m} \tag{1}$$

where A is the integral area of the cyclic voltammogram loop, ΔV is the sweep potential window, ν is the scan rate and m is the mass of the electrode materials at each electrode. Alternatively, the specific capacitance was calculated from the galvanostatic charge–discharge curve according to the following equation [3,29]

$$C = 2 \times \frac{I \times \Delta t}{\Delta V \times m} \tag{2}$$

where I is the applied discharge current, Δt is the discharged time after IR drop. Factor of 2 was used because the series capacitance was formed in a two-electrode system. The energy density (E) and the power density (P) were expressed as [3,29]

$$E(Wh/kg) = \frac{1}{2}C\Delta \nu^2 \times \frac{1000}{3600} \tag{3}$$

$$P(W/kg) = \frac{E}{\Delta t} = \frac{I\Delta V}{2m} \times 1000 \tag{4}$$

where C is the specific capacitance calculated from the charge–discharge curves.

3. Results and discussion

Fig. 1 shows the TEM and SEM images taken from the rGO sheets and the rGO–Co_3O_4 composite. 20 nm sized Co_3O_4 nanoparticles were well dispersed on the rGO sheet surface. The HRTEM image taken from a single Co_3O_4 nanoparticle shows the lattice fringe with a d spacing of 0.285 nm, which corresponds to the (220) plane of Co_3O_4. The TGA measurement showed that about 7.2 wt% of cobalt oxide was deposited onto the rGO sheets. The BET measurement revealed that the specific surface areas of the rGO and the rGO–Co_3O_4 composite were 619.5 m^2 g^{-1} and 112.9 m^2 g^{-1}, respectively. Fig. 2(a) shows the XRD pattern of the as-prepared rGO–Co_3O_4 composite. A peak at 24.7° was characteristic of the (002) peak of rGO [30]. All other peaks can be assigned to the crystalline Co_3O_4 according to the JCPDS card No. 71-0816. Fig. 2(b) shows the Raman spectrum of the rGO–Co_3O_4 composite. The peaks at 1350 cm^{-1} and 1593 cm^{-1} were attributed to sp^3 (D band) and sp^2 (G band) hybridization carbon atoms, respectively. Four peaks at 188, 469, 515 and 676 cm^{-1} were ascribed to the F_{2g}, E_g, F_{2g} and A_{1g} modes in Co_3O_4, respectively [31].

As shown in the FT-IR spectra (see Figure S1), GO possessed abundant oxygen-containing functional groups such as hydroxyl
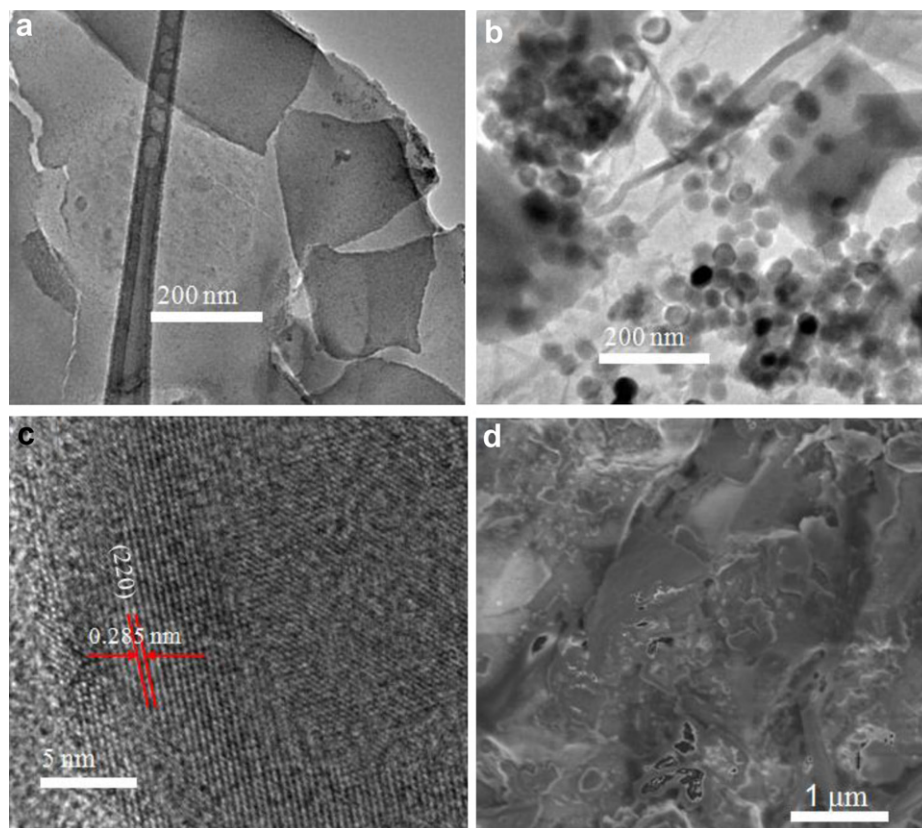
Fig. 1. TEM images of (a) reduced graphene oxide (rGO) and (b) the rGO−Co$_3$O$_4$ composite, (c) high resolution TEM image of the rGO−Co$_3$O$_4$ composite, and (d) SEM image of the rGO−Co$_3$O$_4$ composite.
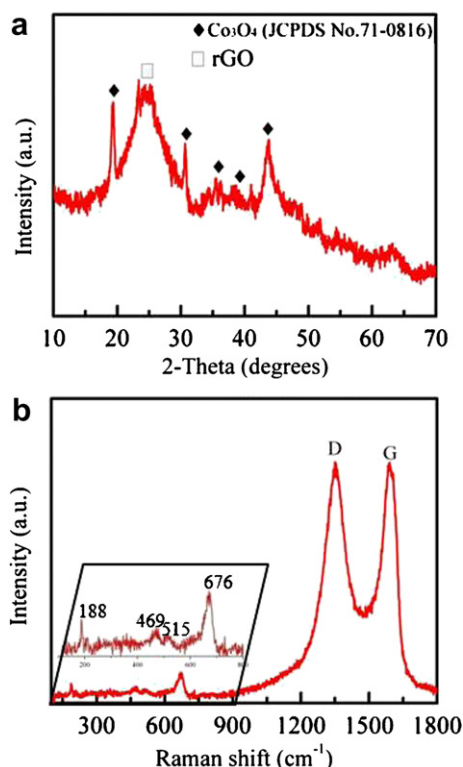

Fig. 2. (a) XRD pattern and (b) Raman spectrum of the rGO−Co$_3$O$_4$ composites.

group, epoxide, carbonyl and carboxyl groups [32−35], which enabled the covalent binding of metal oxides. Previous studies have demonstrated that the hydrothermal treatment in ethanol can reduce GO to rGO [3,36]. Consistently, our results also show the significant decrease in the C=O peak intensity in the FT-IR spectrum after hydrothermal treatment, indicating the reduction of GO.

Fig. 3 shows XPS spectra of the rGO−Co$_3$O$_4$ composite. The C 1s core level spectrum contained three components at 284.8 eV, 286.2 eV and 288.6 eV, which were assigned to the C−C or C=C bonds, C−O bond and C=O bond, respectively [32,37]. This indicated that the oxygen-containing functional groups still existed on the carbon ring skeleton. The XPS spectra of the Co 2p core level confirmed that cobalt existed in the form of Co$_3$O$_4$. In short, the detailed microscopic and spectroscopic results confirmed the successful deposition of the Co$_3$O$_4$ nanoparticles onto the rGO sheets.

Fig. 4(a) presents the CV curves of the rGO and the rGO−Co$_3$O$_4$ composite electrodes at a sweep potential window of 0−0.85 V at a scan rate of 100 mV s^{-1}. The rectangular area of the CV loop was significantly enhanced by the introduction of Co$_3$O$_4$ onto the rGO sheets. The enhancement was mainly ascribed to the pseudocapacitance of the electrochemically active Co$_3$O$_4$. In the redox process, two sequential reactions take place as follows: [38]

$$Co_3O_4 + OH^- + H_2O \leftrightarrow 3CoOOH + e^-$$

$$CoOOH + OH^- \leftrightarrow CoO_2 + H_2O + e^-$$
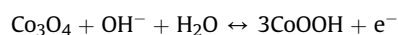
The CV loop was close to a rectangular shape, which was desirable for a supercapacitor. The rate capability was examined by measuring the CV response at various scan rates (2, 5, 10, 25, 50 and
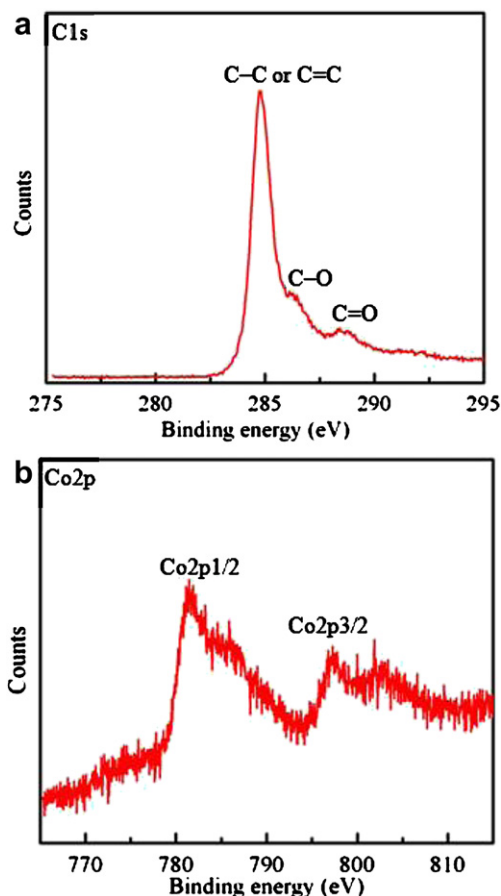
Fig. 3. (a) C 1s and (b) Co 2p core level XPS spectra obtained from the rGO–Co_3O_4 composite.

100 mV s^{-1}) as shown in Fig. 4(b). The rectangular area increased with increasing the scan rate. Fig. 4(c) shows the plots of specific capacitances of the rGO and the rGO–Co_3O_4 composite electrodes as a function of the scan rate. The specific capacitance of the rGO–Co_3O_4 composite electrode was significantly larger than that of the rGO electrode at all scan rates. The specific capacitance slightly decreased with an increase in the scan rate. The specific capacitance of the rGO–Co_3O_4 composite was about 472 F g^{-1} at a scan rate of 2 mV s^{-1} while the specific capacitance of rGO was about 44 F g^{-1}. Generally, the rate capability is heavily dependent on three processes [11,39]: the ion diffusion in the electrolyte, the surface adsorption of ions on the electrode materials and the charge transfer in the electrode. At a high scan rate, any of three processes is relatively slow, which will limit the rate, lowering the specific capacitance. 82.6% of capacitance remained when the scan rate reached 100 mV s^{-1}. This indicated higher rate capability of the rGO–Co_3O_4 composite as compared to the carbon-metal oxide composite electrode reported previously [40]. Such good rate capability was attributed to the advantages of the rGO–Co_3O_4 composite. Small sized Co_3O_4 particles resulted in high specific pseudocapacitance. Although the rGO sheets make small contribution to the specific capacitance of the rGO/Co_3O_4 composite, they have excellent electronic conductivity and thus shuttle the electrons between the Co_3O_4 particles and the current collector. Therefore, integration of Co_3O_4 with rGO into a single system enhanced the electrochemical behavior of supercapacitor electrode.

Electrochemical impedance spectroscopy (EIS) spectra were obtained to characterize the composite electrode. Fig. 4(d) reveals the Nyquist plots of the rGO and the rGO–Co_3O_4 composite electrodes. The rGO electrodes exhibited almost vertical line at the low-frequency region, indicating the desired capacitive behavior. The electrode series resistance (R_s) was derived from the high frequency intersection of the Nyquist plot in the real axis. It was found that the rGO–Co_3O_4 composite had the similar series resistance to rGO, which confirmed that the superior electronic
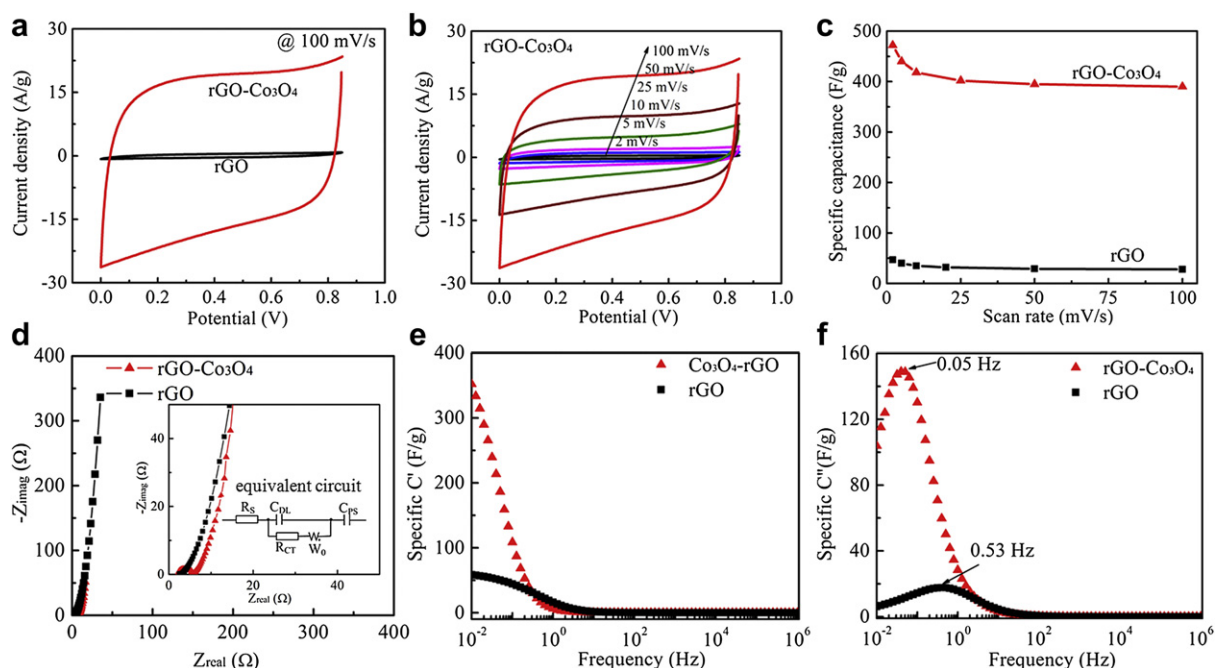

Fig. 4. (a) Cyclic voltammetric curves of the rGO and rGO–Co_3O_4 composite electrodes at a scan rate of 100 mV s^{-1}, (b) cyclic voltammetric curves of the rGO–Co_3O_4 composite electrode at various scan rates (2, 5, 10, 25, 50 and 100 mV s^{-1}), (c) plots of specific capacitance of rGO and rGO–Co_3O_4 composite electrodes as a function of scan rate, (d) Nyquist plots of the rGO and rGO–Co_3O_4 composite electrodes, the inset shows the zoom-in of Nyquist plots and the equivalent circuit, and Bode plots of (e) real and (f) imaginary parts of specific capacitance of the rGO and rGO–Co_3O_4 composite electrodes.

conductivity of rGO was preserved after loading of Co_3O_4. In addition, no semi-arc was observed in the impedance spectrum for the rGO electrode. In contrast, a small semi-arc was found for the rGO–Co_3O_4 composite electrode, which was originated from the charge transfer process of the pseudocapacitive Co_3O_4. The charge transfer resistance (R_{CT}) was estimated to be 3.4 Ω for the rGO–Co_3O_4 composite. The small charge transfer resistance was due to the following facts: (i) the size of Co_3O_4 particles was so small that the electron path-length was short, and (ii) the well-dispersed Co_3O_4 particles were in intimate contact with highly conductive rGO sheets, which minimized the interfacial resistance of the charge transfer process. The frequency-dependent response of supercapacitance can be analyzed from the EIS spectra. Fig. 4(e and f) shows the Bode plots of real and imaginary parts of rGO and rGO–Co_3O_4 composite electrodes, respectively. The specific capacitance increased with a decrease in the frequency at the low-frequency region (Fig. 4(e)). The rGO–Co_3O_4 composite electrode exhibited much higher specific capacitance than the rGO electrode in the frequency range of 0.01–1 Hz. The response time ($\tau = 1/f_m$) of the supercapacitor electrode can be obtained from the Bode plot of imaginary part (C'') of specific capacitance (Fig. 4(f)). The frequency (f_m) corresponded to the maximum of the Bode plots of the imaginary capacitance. The response time was estimated to be 20 s for the rGO–Co_3O_4 composite electrode, which was larger than that (1.9 s) of the rGO electrode. The increase in the response time was due to larger RC constant in the rGO–Co_3O_4 composite. Since the series resistance R_s almost kept constant in rGO and rGO–Co_3O_4, the increase in the response time of the rGO–Co_3O_4 composite electrode should be ascribed to significant increase in the specific capacitance.

Fig. 5 depicts the galvanostatic charge–discharge behaviors of the rGO and the rGO–Co_3O_4 composite electrodes between 0 and 0.85 V at different current densities. Both rGO and rGO–Co_3O_4 electrodes exhibited a good symmetric shape with the coulomb efficiency close to 1. The rGO–Co_3O_4 composite electrode showed longer charge–discharge time than the rGO electrode, indicating larger specific capacitance (Fig. 5(a and b)). The specific capacitance of the rGO–Co_3O_4 electrode was investigated with the progressively increasing current density (Fig. 5(c)). The specific capacitance was reduced from 458 F g^{-1} to 416 F g^{-1} with an increase in the current density from 0.5 A g^{-1} to 2.0 A g^{-1}. The long-term stability of the rGO–Co_3O_4 electrode was also investigated at the current density of 2 A g^{-1}. The specific capacitance of the rGO–Co_3O_4 electrode increased during the first 100 cycles, which was due to an activation process in the supercapacitor electrode, similar to the previous report [40]. About 95.6% of the specific capacitance of rGO–Co_3O_4 electrode was retained at the current density of 2.0 A g^{-1} after 1000 cycles (Fig. 5(d)), which demonstrated high cycling stability.

Fig. 6 shows the Ragone plots of the rGO and the rGO–Co_3O_4 composite electrodes. The energy density and the power density were calculated based on the mass of electrode materials in single electrode. The rGO electrode delivered energy density as low as 4.7 Wh kg^{-1} even at a low-level power density (19.9 W kg^{-1}) because of its low specific capacitance. In contrast, the rGO–Co_3O_4 composite supercapacitor showed significant enhancement in both the energy density and the power density. It delivered an energy density of 47.2 Wh kg^{-1} at the power density of 200.6 W kg^{-1}. More importantly, the energy density was very stable with the increase in the power density. The energy density reached up to 39.0 Wh kg^{-1} even at a power density as high as 8.3 kW kg^{-1}, which was much higher than most of current commercial supercapacitors [8]. As mentioned in the previous sections, the rGO–Co_3O_4 composite electrode had high specific capacitance which can store high density energy. The charge transfer and series resistance are small due to the combination of the Co_3O_4 nanoparticles with the rGO sheets. The excellent rate capability of the rGO–Co_3O_4 electrode
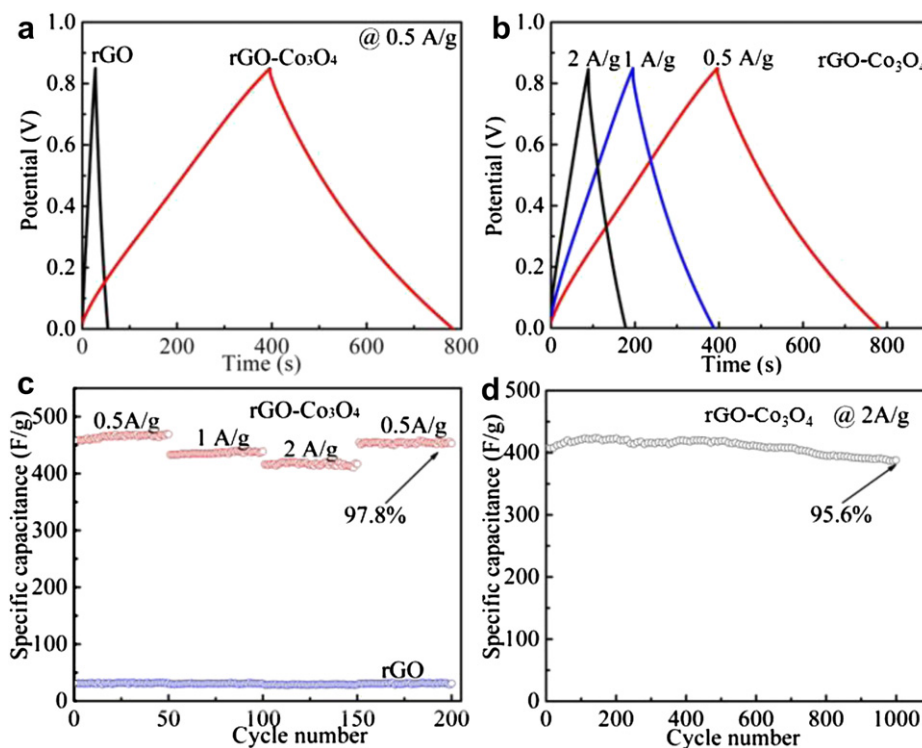

Fig. 5. (a) Charge–discharge curves of the rGO and the rGO–Co_3O_4 composite electrodes at the current density of 0.5 A g^{-1}, (b) charge–discharge curves of the rGO–Co_3O_4 composite electrodes at different current densities (0.5, 1.0 and 2.0 A g^{-1}), (c) cycling stability of rGO–Co_3O_4 composite electrodes upon progressively varying the current density, and (d) long-term stability of the rGO–Co_3O_4 composite electrode upon charge/discharge at a current density of 2.0 A g^{-1}.
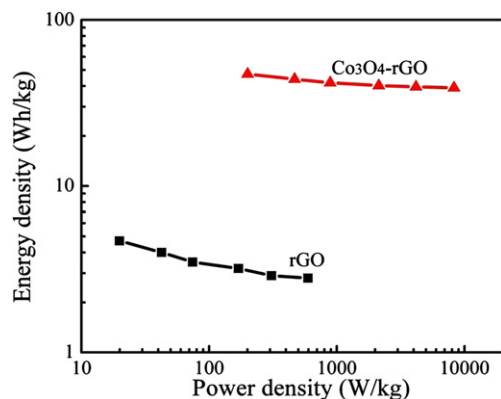
Fig. 6. Ragone plots of the rGO and the rGO—Co$_3$O$_4$ composite electrodes. The energy density and the power density were derived from the charge/discharge curves at various current densities.

ensures that it can efficiently deliver energy at short discharge time and high discharge current with negligible polarization and *IR* loss, and thus a high energy density can be achieved at relatively high power density.

4. Conclusions

This work has demonstrated a facile method for synthesis of the rGO—Co$_3$O$_4$ composite for supercapacitor electrode. The rGO—Co$_3$O$_4$ composite electrode showed much higher specific capacitance than the rGO electrode due to the redox activity of the Co$_3$O$_4$ nanoparticles. The rGO—Co$_3$O$_4$ composite electrode exhibited high energy density at high-level power density, which was attributed to the combination of high pseudocapacitance of Co$_3$O$_4$ with high electronic conductivity of the rGO sheets. The energy density reached 39.0 Wh kg^{-1} even at a power density of 8.3 kW kg^{-1}. The rGO—Co$_3$O$_4$ composite electrode showed high rate capability and excellent long-term stability. 95.6% of initial capacitance was retained after 1000 cycles of continuous operation at a current density of 2.0 A g^{-1}.

Acknowledgment

Appendix A. Supplementary data

Supplementary data related to this article can be found at http://dx.doi.org/10.1016/j.jpowsour.2012.10.064.

References

[1] M. Winter, R.J. Brodd, Chem. Rev. 104 (2004) 4245—4269.
[2] L.L. Zhang, X.S. Zhao, Chem. Soc. Rev. 38 (2009) 2520—2531.
[3] C. Xiang, M. Li, M. Zhi, A. Manivannan, N.Q. Wu, J. Mater. Chem. 22 (2012) 19161—19167.
[4] X. Huang, X. Qi, F. Boey, H. Zhang, Chem. Soc. Rev. 41 (2012) 666—686.
[5] Y. Wang, Z. Shi, Y. Huang, Y. Ma, C. Wang, M. Chen, Y. Chen, J. Phys. Chem. C 113 (2009) 13103—13107.
[6] J. Xu, K. Wang, S.-Z. Zu, B.-H. Han, Z. Wei, ACS Nano 4 (2010) 5019—5026.
[7] X. Cao, Y. Shi, W. Shi, G. Lu, X. Huang, Q. Yan, Q. Zhang, H. Zhang, Small 7 (2011) 3163—3168.
[8] A. Burke, J. Power Sources 91 (2000) 37—50.
[9] A.M. van Voorden, L.M.R. Elizondo, G.C. Paap, J. Verboomen, L. van der Sluis, in: IEEE Power Tech. Conference, 2007, pp. 479—484.
[10] M. Zhi, A. Manivannan, F. Meng, N.Q. Wu, J. Power Sources 208 (2012) 345—353.
[11] J. Li, W. Zhao, F. Huang, A. Manivannan, N.Q. Wu, Nanoscale 3 (2011) 5103—5109.
[12] V. Subramanian, H. Zhu, R. Vajtai, P.M. Ajayan, B. Wei, J. Phys. Chem. B 109 (2005) 20207—20214.
[13] J. Jiang, J. Liu, R. Ding, J. Zhu, Y. Li, A. Hu, X. Li, X. Huang, ACS Appl. Mater. Interfaces 3 (2011) 99—103.
[14] J. Liu, J. Jiang, C. Cheng, H. Li, J. Zhang, H. Gong, H.J. Fan, Adv. Mater. 23 (2011) 2076—2081.
[15] Z. Chen, V. Augustyn, J. Wen, Y. Zhang, M. Shen, B. Dunn, Y. Lu, Adv. Mater. 23 (2011) 791—795.
[16] Q. Qu, P. Zhang, B. Wang, Y. Chen, S. Tian, Y. Wu, R. Holze, J. Phys. Chem. C 113 (2009) 14020—14027.
[17] W. Tang, Y.Y. Hou, X.J. Wang, Y. Bai, Y.S. Zhu, H. Sun, Y.B. Yue, Y.P. Wu, K. Zhu, R. Holze, J. Power Sources 197 (2012) 330—333.
[18] W. Lu, R. Hartman, L. Qu, L. Dai, J. Phys. Chem. Lett. 2 (2011) 655—660.
[19] A. Ghosh, E.J. Ra, M. Jin, H.-K. Jeong, T.H. Kim, C. Biswas, Y.H. Lee, Adv. Funct. Mater. 21 (2011) 2541—2547.
[20] W. Tang, L. Liu, S. Tian, L. Li, Y. Yue, Y. Wu, K. Zhu, Chem. Commun. 47 (2011) 10058—10060.
[21] Q. Qu, Y. Zhu, X. Gao, Y. Wu, Adv. Energy Mater. 2 (2012) 950—955.
[22] M.N. Hyder, S.W. Lee, F.C. Cebeci, D.J. Schmidt, Y. Shao-Horn, P.T. Hammond, ACS Nano 5 (2011) 8552—8561.
[23] P.-C. Chen, G. Shen, Y. Shi, H. Chen, C. Zhou, ACS Nano 4 (2010) 4403—4411.
[24] A. Izadi-Najafabadi, S. Yasuda, K. Kobashi, T. Yamada, D.N. Futaba, H. Hatori, M. Yumura, S. Iijima, K. Hata, Adv. Mater. 22 (2010) E235—E241.
[25] J. Yan, W. Qiao, B. Shao, Q. Zhao, L. Zhang, Z. Fan, Electrochim. Acta 55 (2010) 6973—6978.
[26] W.S. Hummers, R.E. Offeman, J. Am. Chem. Soc. 80 (1958). 1339—1339.
[27] J. Zhang, H. Yang, G. Shen, P. Cheng, J. Zhang, S. Guo, Chem. Commun. 46 (2010) 1112—1114.
[28] M. Salari, S.H. Aboutalebi, K. Konstantinov, H.K. Liu, Phys. Chem. Chem. Phys. 13 (2011) 5038—5041.
[29] Q. Wu, Y. Xu, Z. Yao, A. Liu, G. Shi, ACS Nano 4 (2010) 1963—1970.
[30] Y. Zou, Y. Wang, ACS Nano 5 (2011) 8108—8114.
[31] J. Yang, H. Liu, W.N. Martens, R.L. Frost, J. Phys. Chem. C 114 (2010) 111—119.
[32] M. Li, S.K. Cushing, X. Zhou, S. Guo, N.Q. Wu, J. Mater. Chem. 22 (2012) 23374—23379.
[33] N.Q. Wu, L. Fu, M. Su, M. Aslam, K.C. Wong, V.P. Dravid, Nano Lett. 4 (2004) 383—386.
[34] M. Lim, K. Feng, X. Chen, N.Q. Wu, A. Raman, E.S. Gawalt, J. Nightingale, D. Korakakis, L.A. Hornak, A. Timperman, Langmuir 23 (2007) 2444—2452.
[35] Y. Zhu, X. Li, Q. Cai, Z. Sun, G. Casillas, M. Jose-Yacaman, R. Verduzco, J.M. Tour, J. Am. Chem. Soc. 134 (2012) 11774—11780.
[36] Y. Zhang, Z.-R. Tang, X. Fu, Y.-J. Xu, ACS Nano 4 (2010) 7303—7314.
[37] S. Stankovich, R.D. Piner, X. Chen, N.Q. Wu, S.T. Nguyen, R.S. Ruoff, J. Mater. Chem. 16 (2006) 155—158.
[38] X.-C. Dong, H. Xu, X.-W. Wang, Y.-X. Huang, M.B. Chan-Park, H. Zhang, L.-H. Wang, W. Huang, P. Chen, ACS Nano 6 (2012) 3206—3213.
[39] Y. Zhang, G. Li, Y. Lv, L. Wang, A. Zhang, Y. Song, B. Huang, Int. J. Hydrogen Energy 36 (2011) 11760—11766.
[40] H. Jiang, J. Ma, C. Li, Chem. Commun. 48 (2012) 4465—4467.